Journal of Power Sources 696 (2026) 241459

Contents lists available at ScienceDirect

Journal of Power Sources

journal homepage: www.elsevier.com/locate/jpowsour

Understanding electro-chemo-mechanical stresses in ceria-based solid oxide electrolysis cells using virtual microstructures

Lukas Schöller [a,b,*], Luzie Wehner [c], Denise Ramler [d], Iurii Kogut [e], Stefan Kucharski [d], Christian Lenser [d], Ravi Kumar Jeela [a,b], Daniel Schneider [a,b,f], André Weber [e], Ruth Schwaiger [c], Britta Nestler [a,b,f]

[a] Institute of Digital Materials Science (IDM), Karlsruhe University of Applied Sciences, Moltkestraße 30, 76133 Karlsruhe, Germany
[b] Institute for Applied Materials – Microstructure Modelling and Simulation (IAM-MMS), Karlsruhe Institute of Technology (KIT), Kaiserstraße 12, 76131 Karlsruhe, Germany
[c] Institute of Energy Materials and Devices: Structure and Function of Materials (IMD-1), Forschungszentrum Jülich GmbH, Wilhelm-Johnen-Straße, 52428 Jülich, Germany
[d] Institute of Energy Materials and Devices: Materials Synthesis and Processing (IMD-2), Forschungszentrum Jülich GmbH, Wilhelm-Johnen-Straße, 52428 Jülich, Germany
[e] Institute for Applied Materials – Electrochemical Technologies (IAM-ET), Karlsruhe Institute of Technology (KIT), Kaiserstraße 12, 76131 Karlsruhe, Germany
[f] Institute of Nanotechnology – Microstructure Simulations (INT-MSS), Karlsruhe Institute of Technology (KIT), Hermann-von-Helmholtz-Platz 1, 76344 Eggenstein-Leopoldshafen, Germany

HIGHLIGHTS

- Generate virtual microstructures to use in mechanical simulations for SOEC.
- Facile modification of the microstructure of single layers, and assessment of the resulting changes in cell properties.
- Develop exemplary design rules for the SOEC investigated in this work.

GRAPHICAL ABSTRACT

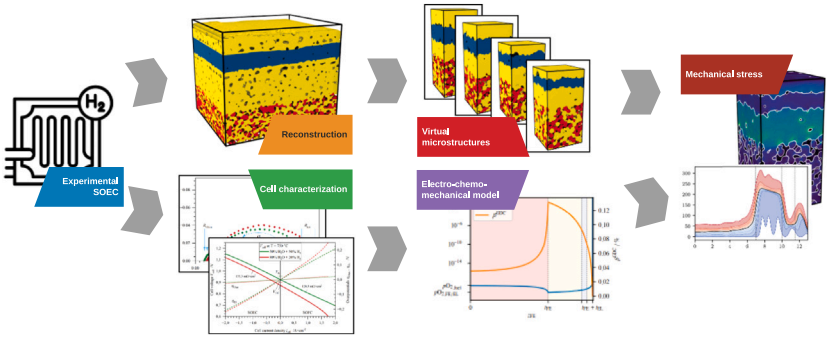

ARTICLE INFO

Keywords:
Solid oxide electrolysis cell
Ceria-based electrolyte
Electro-chemo-mechanical modeling
Virtual microstructures
Phase-field modeling

ABSTRACT

Solid oxide electrolysis cells (SOEC) based on a thin ceria electrolyte show excellent performance, but suffer from mechanical instability due to expansion of the ceria electrolyte. The cathodic overpotential of the fuel electrode increases the chemical expansion, which couples the expansion to the operation conditions and can lead to electro-chemo-mechanical failure of the cell. Among the possible mitigation strategies is the optimization of the microstructure to minimize chemical stresses during operation. However, changing individual features of the microstructure experimentally can be extremely time-consuming and even impossible, as the cell production couples the microstructure evolution of support, electrode and electrolyte during sintering. Here, we present an innovative approach using a microstructure generator to tailor synthetic microstructures and examine the influence of microstructural parameters, such as particle size, density, or

* Corresponding author at: Institute for Applied Materials – Microstructure Modelling and Simulation (IAM-MMS), Karlsruhe Institute of Technology (KIT), Kaiserstraße 12, 76131 Karlsruhe, Germany.
E-mail addresses: lukas.schoeller@kit.edu (L. Schöller), l.wehner@fz-juelich.de (L. Wehner), d.ramler@fz-juelich.de (D. Ramler), iurii.kogut@kit.edu (I. Kogut), s.kucharski@fz-juelich.de (S. Kucharski), c.lenser@fz-juelich.de (C. Lenser), ravi_kumar.jeela@h-ka.de (R.K. Jeela), daniel.schneider@kit.edu (D. Schneider), andre.weber@kit.edu (A. Weber), r.schwaiger@fz-juelich.de (R. Schwaiger), britta.nestler@kit.edu (B. Nestler).

https://doi.org/10.1016/j.jpowsour.2026.241459
Received 6 March 2026; Received in revised form 29 June 2026; Accepted 6 September 2026
Available online 17 September 2026

electrolyte thickness, on the predicted mechanical stresses during operation. This approach yields correlations between microstructure and chemical stresses with greatly reduced effort compared to an experimental approach, and highlights the potential of digital materials design.

1. Introduction

Solid oxide electrolysis cells (SOEC) enable the production of hydrogen or syngas with high electrical efficiency (100 % cell efficiency when operated at the thermoneutral voltage), making them an attractive technology to realize sector coupling between the electrical and chemical sector. Compared to fuel cell operation (power generation mode), SOEC using a Ni/$Y_{0.148}Zr_{0.852}O_{1.93}$ (8YSZ) electrode suffers from a specific degradation mechanism linked to the migration of Ni away from the electrolyte, mostly driven by the electrode overpotential [1–3]. As a result, the degradation in SOEC mode is higher than in SOFC operation [4,5]. In contrast, cells utilizing a cermet electrode made from Ni and doped ceria, e.g. $Gd_{0.1}Ce_{0.9}O_{1.95-}$ (GDC), show lower degradation rates under harsh conditions [6]. The manufacturing sequence and required sintering temperatures have so far restricted Ni/GDC electrodes to electrolyte- and metal-supported cells, since co-firing of half-cell results in severe interdiffusion between GDC and YSZ that is detrimental to cell performance [7]. However, recent efforts to incorporate Ni/GDC electrodes into fuel-electrode supported cells have yielded promising results when using a Physical Vapor Deposition (PVD) layer to avoid interdiffusion [8], or when reducing the sintering temperature to minimize it [9]. The use of a GDC electrolyte layer co-fired with the Ni/GDC electrode avoids the formation of GDC-YSZ mixed phases or Kirkendall voids at the electrode-electrolyte interface [10]. While the resulting cell performance is excellent, there are issues with the mechanical stability of the electrolyte that have been hypothesized to derive from electro-chemo-mechanical stresses resulting from the expansion of the ceria layer under the strongly reducing conditions of the SOEC cathode overpotential [11]. In order to understand and mitigate the mechanical degradation of the cell via electro-chemo-mechanical coupling, we investigate the mechanical stresses in the cell as a function of the operational parameters and the cell's microstructure. Experimental modifications of the microstructure are very labor-intensive to implement and often have undesired side-effects. For instance, changing the electrolyte thickness will change the curvature of the cell after sintering, possibly preventing electrochemical characterization and potentially changing residual stresses in the system. Therefore, we utilize virtual microstructures generated via dense sphere packing based on discrete particle packing and spherical-harmonics [12]. The starting point is a microstructure designed to align with an experimental three-dimensional structure reconstructed via FIB milling and SEM imaging regarding layer thicknesses, volume fractions, and porosity. The virtual microstructure can be easily modified, so the structure generator is used to investigate how different microstructures affect the mechanical stresses in the cell. In order to achieve this, we developed a model that predicts the local mechanical stresses in the cell in dependency of the local oxygen partial pressure pO_2 in all three dimensions. Prerequisites for these calculations are reliable input parameters under SOEC conditions (high temperature, low pO_2):

- Mechanical parameters, such as the Young's modulus
- Chemical expansion of ceria under cathodic polarization
- Three-dimensional representation of the microstructure of the cell
- Quantification of the overpotential and its distribution to anode, cathode and electrolyte

We address each of these prerequisites with dedicated experiments that supply the necessary information for the model.

This paper is structured as follows. Section 2 details the workflow, including cell manufacturing and characterization, three-dimensional microstructure reconstruction, the chemo-mechanical multiphasefield framework and governing equations, the treatment of oxygen partial pressure, and the generation of virtual microstructures. Section 3 begins with the generated microstructure, the choice of boundary conditions, and the discussion of the stress distribution in an exemplary microstructure, followed by systematic studies of operating conditions (e.g., fuel-electrode overpotential) and morphology (e.g., electrolyte thickness and porosity). Finally, Section 4 summarizes the main findings and outlines implications for microstructure design and operating parameters.

2. Methods

This Section introduces the methods used to compute local mechanical stresses in ceria-based SOECs at operating temperature and low oxygen partial pressure. The subsections cover cell manufacturing and characterization, microstructure reconstruction, the multiphase-field method for chemo-mechanical coupling, generation of virtual microstructures, and the distribution of oxygen partial pressure in the electrolyte, forming an experimental-computational workflow for the subsequent analyses. It must be pointed out that for the entire analysis presented in this paper, the influence of the air electrode is neglected. This is motivated by the extremely small overpotential of LSC electrodes at the investigated conditions, which amounts to approximately 10 % of the total overpotential in these cells [13], as well as their very low mechanical stiffness. This combination suggests that the influence of the air electrode on the calculations presented here is very small, but would be computationally demanding due to their small particle size and the overall increase in the volume of the investigated microstructures.

2.1. Cell manufacturing

Two types of fuel electrode-supported cells were manufactured for the microstructure reconstruction and electrochemical cell characterization presented in this work: (i) a fully suspension-based cell and (ii) a cell employing two PVD-derived barrier layers. Both cell types share the same underlying architecture. The support consists of an in-house tape-cast NiO/8YSZ substrate (NiO: Green Nickel Oxide, Vogler, the Netherlands and 8YSZ: $Y_{0.148}Zr_{0.852}O_{1.93}$, Unitec Ceramics Ltd., U.K.), pre-calcined prior to subsequent processing. A NiO/10GDC ($Gd_{0.10}Ce_{0.90}O_{1.95-\delta}$, 10GDC-M, Fuelcellmaterials, USA) fuel electrode functional layer was applied by screen printing using a semi-automatic screen printer (EKRA E2, EKRA Automatisierungssysteme GmbH, Germany). The electrolyte for both cell types is a three-layer design: a 10GDC electrolyte layer, a 8YSZ (TZ-8Y, Tosoh, Japan) barrier layer to suppress electronic conduction, and a top 10GDC barrier layer to inhibit strontium zirconate formation at the air-electrode/8YSZ-interface. The manufacturing routes differ only in the fabrication of the electrolyte. In the fully suspension-based cell, all electrolyte layers are screen-printed and co-sintered at 1400 °C for 5 h. In contrast, for the PVD-processed cell only the first GDC layer was screen-printed and sintered at 1400 °C, after which the approximately 500 nm thick YSZ and GDC barrier layers were deposited separately by reactive magnetron sputtering (CS400ES cluster system, Von Ardenne Anlagentechnik GmbH, Germany). These distinct fabrication procedures resulted in pronounced differences in microstructure and subsequent cell performance, motivating the range of virtual barrier-layer configurations investigated in this study. In the fully screen-printed cell, all electrolyte layers were formed by suspension-based processing and co-sintering, whereas the PVD-processed cell contains thin, separately

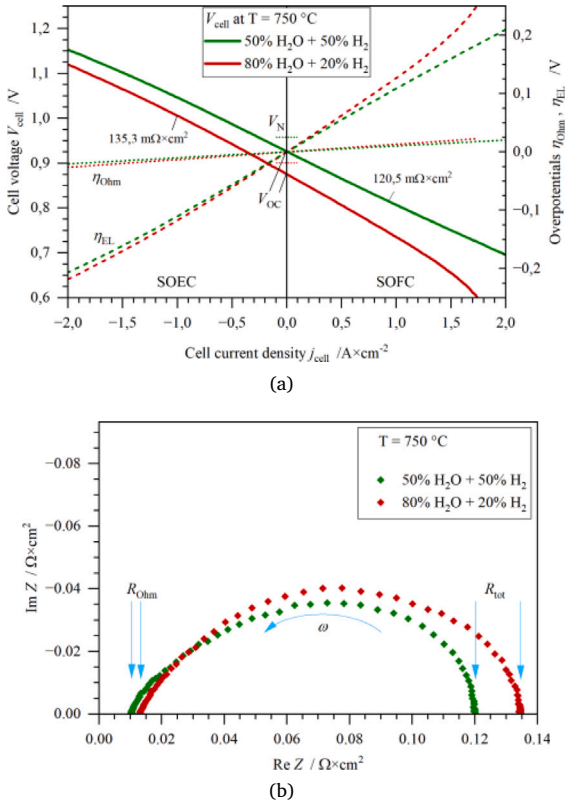

Fig. 1. Current–voltage characteristics (a) and impedance spectra (b) of the modeled SOEC at 750 °C and H_2O in the fuel, and extraction of overpotentials for parametrizing the model.

deposited YSZ and GDC barrier layers. Particularly with respect to layer thicknesses, which were larger for screen-printed layers (>4 μm) and the quality of interfaces. The fully screen-printed cells exhibited significant interface porosity within the electrolyte, whereas the PVD-derived barrier layers produced clear and distinct interfaces with no porosity. For cell tests, either lanthanum-strontium-cobalt-ferrite (LSCF) or lanthanum-strontium-cobaltite (LSC) air electrodes were printed on top of the electrolyte.

The FIB/SEM reconstruction used as morphological reference for the virtual microstructure generation was obtained from the fully screen-printed cell. In contrast, the electrochemical boundary conditions used for the mechanical simulations, summarized in Fig. 1 and Table 1, were derived from measurements on the PVD-processed cell. The use of different experimental inputs is deliberate. The fully screen-printed cell provides the morphological reference for the virtual structures, because it contains the thicker suspension-derived electrolyte-stack geometry relevant for the present parameter study. The PVD-processed cell, in contrast, provides electrochemical boundary conditions from a cell with thinner, separately deposited barrier layers that were not co-sintered with the electrolyte stack after deposition. Extended GDC/YSZ interdiffusion zones are therefore expected to be negligible compared with the fully screen-printed cell. Since such interdiffusion zones are not explicitly represented in the present model and reliable material parameters for them are not available, the PVD-derived electrochemical data provide a better-defined operating condition for the mechanical simulations.

2.2. Cell characterization

To simulate the mechanical response of synthetic SOECs during operation, realistic electrochemical boundary conditions were derived

Table 1
Electrochemical parameters for the representative operation points of the SOEC extracted from electrochemical characterization.

H_2O content	V_N	V_{OC}	R_{Ohm}	j_{cell}	η_{EL}	R_{pol}
mol %	V	V	mΩ cm²	A cm⁻²	V	mΩ cm²
50	0.9574	0.9258	10.2	0.0	0.0	–
				−0.5	−0.0559	111.8
				−1.0	−0.1100	110.0
				−1.5	−0.1606	107.1
				−2.0	−0.2065	103.3
80	0.8963	0.8755	13.1	0.0	0.0	–
				−0.5	−0.0603	120.6
				−1.0	−0.1172	117.2
				−1.5	−0.1697	113.1
				−2.0	−0.2181	109.5

from electrochemical impedance spectra (EIS) and current–voltage characteristics (IV-curves) of GDC-based cells. These were measured following the characterization procedures described in [14,15]. A more extensive study of the cells will be published separately. In brief, the cells were characterized at temperatures of 600–800 °C under a pO_2 gradient set by dry laboratory compressed air ($pO_2 \approx 0.21$ bar) and fuel gas composed of 5–80 mol % steam balanced in H_2. Both gas streams were supplied at a flow rate of 0.25 L min^{-1} to the air electrode (AE) and the fuel electrode (FE) support, respectively. The AE and FE were contacted using 1 cm^2 square gold and nickel current-collecting meshes, which allow unobstructed gas access to the electrochemically active regions of the porous electrodes. EIS measurements were performed under open-circuit conditions using a Solartron SI1260 impedance/gain-phase analyzer with galvanostatic perturbation. The AC amplitude was adjusted to ensure a voltage response $\leq$ 12 mV. Sweep frequencies ranged from 0.05 Hz to 1 MHz, covering relaxation times characteristic of most processes occurring in SOEC electrodes. IV-curves were measured in both fuel cell and electrolysis modes by applying DC currents up to ±2 A cm^{-2} using an Agilent 6612C DC power supply, in increments of 20 mA cm^{-2} with an integration time of 20 s per step. Voltage signals were recorded with an Agilent 34970 A data acquisition unit. The measured IV-curves are almost linear under SOEC mode polarization, and the open-circuit voltage ($V_{OC}, j_{cell} = 0$ A cm^{-2}, see Fig. 1(a)) is lower than the theoretical Nernstian value V_N for the given H_2:H_2O ratios, although the deviation is smaller in a more oxidizing fuel atmosphere (80 mol % H_2O). The lower measured open-circuit voltage compared with the theoretical Nernstian value is consistent with partial electronic conduction in the reduced GDC, which partially relaxes the oxygen chemical-potential gradient across the electrolyte, and with finite electron blocking efficiency of the 8YSZ layer. The latter may result from the finite YSZ thickness and local microstructural imperfections, for example defects in the underlying screen-printed electrolyte that are not fully covered by the thin PVD layer. At such sites, localized electronic short-circuit paths or gas leakage cannot be excluded. In contrast, extended GDC/YSZ interdiffusion is not expected to be a significant contribution in the PVD-processed cell, because the PVD-derived barrier layers were not co-sintered with the electrolyte stack after deposition. A quantitative separation of these contributions is beyond the scope of the present study. The ohmic resistance of the cell is extracted from apparent high-frequency intercepts of the impedance arcs with the real axis in the Nyquist plot (R_{Ohm}, see Fig. 1(b)). If the related ohmic overpotential is assumed linear with respect to applied current ($\eta_{Ohm} = j_{cell} R_{Ohm}$), the total polarization (overpotential) of the electrodes and interfaces is defined as $\eta_{EL} = V_{OC} - V_{cell} - \eta_{Ohm}$, and $R_{pol} = \eta_{EL}/j_{cell}$. If the $\eta_{EL}(j_{cell})$ dependence is considered roughly linear, the corresponding polarization resistance equals $R_{pol} = R_{tot} - R_{Ohm}$, extracted from EIS at V_{OC} (see Fig. 1(b)), and R_{tot} corresponds to the slope of the IV-curve (see Fig. 1(a)). Note that η_{EL} includes contributions from both the fuel electrode and the air electrode. In the present model, these overpotentials η_{FE} and η_{AE} will be

defined by proportional distribution within the total η_{EL}, as suggested in [11]. The boundary electrical parameters defined for the model this way are summarized in Table 1.

For the present mechanical study, the most relevant electrochemical input is the fuel-electrode overpotential, because it determines the reducing conditions and thus the chemical expansion of the fuel-side GDC. The fuel electrode architecture is kept unchanged throughout the virtual parameter studies. The electrochemical parameters obtained from the PVD-processed cell are therefore used as prescribed operating conditions for the controlled morphology variations, rather than as a claim that the virtual structures are direct replicas of the measured PVD cell.

2.3. Microstructure reconstruction

Focused ion beam/scanning electron microscopy (FIB/SEM) tomography is a well-established method for three-dimensional microstructural reconstruction. A consecutive series of images of the volume of interest (VOI) is generated by alternating FIB milling and SEM imaging. A three-dimensional representation of the microstructure and material distribution is obtained by stacking the images, expanding the image pixels in the stacking direction followed by the segmentation. The latter describes the assignment of every voxel to a material phase based on its gray scale value and surrounding material. For the segmentation process, different algorithms have been developed. The watershed algorithm interprets images as topographic reliefs based on every pixel's gray scale value, which corresponds to a height on the image plane. The phase boundaries are stored in an edge map. By flooding the images starting from local minima, every pixel is assigned to a material phase. Preliminary image processing, such as brightness and contrast corrections or noise reduction, and post-processing via morphological filters, e.g. erosion and dilation, are used to avoid and correct segmentation errors [16–18].

For the three-dimensional microstructural reconstruction a series of 313 images was recorded using Helios 5 CXe (Thermo Fisher Scientific, Hillsboro, OR, USA) equipped with a backscattering detector. The VOI ($18\,176\,\mu m^3$) was covered with a mixture of 99 % Pt and 1 % C to protect the microstructure during FIB milling. For image alignment, processing and segmentation Avizo (Version 2023.1.1, Thermo Fischer Scientific, Hillsboro, OR, USA) was used.

2.4. Multiphase-field method

The multiphase-field method (MPFM) is a well-established framework for simulating the evolution of complex microstructures on micro- and mesoscopic length scales. Over the past decades, MPFM has become a standard tool for modeling multi-phase and multi-component systems. For comprehensive reviews of the method and its applications, the reader is referred to [19]. The MPFM employed in this study builds on the formulations of Steinbach et al. [20] and Nestler et al. [21] and includes a mechanical extension following Schneider et al. [22,23]. In contrast to sharp-interface descriptions, MPFM represents interfaces as smooth, diffuse transition regions. The microstructure is described by a set of order parameters $\boldsymbol{\phi} = \{\phi^1, \phi^2, \dots, \phi^N\}$, where each ϕ^α corresponds to one particle (phase). Interpreting the order parameters as local volume fractions imposes the summation constraint

$$\sum_{\alpha=1}^{N} \phi^\alpha = 1. \tag{1}$$

Together with the displacement field $\boldsymbol{u}$ and the spatial gradients $\nabla\boldsymbol{\phi} = \{\nabla\phi^1, \nabla\phi^2, \dots, \nabla\phi^N\}$, the free energy functional of a material body Ω is given by

$$\mathcal{F}[\boldsymbol{u}, \boldsymbol{\phi}] = \int_\Omega \underbrace{f_{\mathrm{grad}}(\nabla\boldsymbol{\phi}) + f_{\mathrm{pot}}(\boldsymbol{\phi})}_{f_{\mathrm{intf}}(\nabla\boldsymbol{\phi},\boldsymbol{\phi})} + f_{\mathrm{el}}(\boldsymbol{u}, \boldsymbol{\phi}, \nabla\boldsymbol{\phi})\, \mathrm{d}v. \tag{2}$$

The interface contribution consists of a gradient term and a potential term,

$$f_{\mathrm{grad}}(\nabla\boldsymbol{\phi}) = -\sum_{\alpha=1}^{N}\sum_{\beta>\alpha}^{N} \gamma^{\alpha\beta} \nabla\phi^\alpha \cdot \nabla\phi^\beta, \tag{3}$$

$$f_{\mathrm{pot}}(\boldsymbol{\phi}) = \frac{16}{\epsilon\pi^2} \sum_{\alpha=1}^{N}\sum_{\beta>\alpha}^{N} \gamma^{\alpha\beta} \phi^\alpha \phi^\beta, \tag{4}$$

where $\gamma^{\alpha\beta}$ is the surface energy between phase α and β, and ϵ controls the diffuse interface width. The phase-specific elastic strain energy density $f_{\mathrm{el}}^\alpha = 1/2\boldsymbol{\sigma}^\alpha \cdot \boldsymbol{\varepsilon}^\alpha$, Cauchy stress tensor $\boldsymbol{\sigma}^\alpha$, and infinitesimal strain tensor $\boldsymbol{\varepsilon}^\alpha$ are interpolated according to

$$\boldsymbol{\sigma} = \sum_{\alpha=1}^{N} \phi^\alpha \boldsymbol{\sigma}^\alpha, \qquad \boldsymbol{\varepsilon} = \sum_{\alpha=1}^{N} \phi^\alpha \boldsymbol{\varepsilon}^\alpha, \qquad f_{\mathrm{el}} = \sum_{\alpha=1}^{N} \phi^\alpha f_{\mathrm{el}}^\alpha, \tag{5}$$

to effective quantities, with $\boldsymbol{\varepsilon} = 1/2\,(\nabla\boldsymbol{u} + \nabla\boldsymbol{u}^{\mathrm{T}})$. The phase-specific strain tensor is additively decomposed into elastic and chemical contributions

$$\boldsymbol{\varepsilon}^\alpha = \boldsymbol{\varepsilon}_{\mathrm{el}}^\alpha + \boldsymbol{\varepsilon}_{\mathrm{ch}}^\alpha \tag{6}$$

and stresses follow Hooke's law

$$\boldsymbol{\sigma}^\alpha = \mathbb{C}^\alpha \left[\boldsymbol{\varepsilon}_{\mathrm{el}}^\alpha\right], \tag{7}$$

with the phase-specific stiffness tensor $\mathbb{C}^\alpha$. Further assumptions are necessary in order to model effective material behavior. Schneider et al. [22,23] amongst others, utilized the mechanical jump conditions

$$[\![\boldsymbol{\varepsilon}]\!]^{\alpha\beta} = \frac{1}{2}\left(\boldsymbol{a}^{\alpha\beta} \otimes \boldsymbol{n}^{\alpha\beta} + \boldsymbol{n}^{\alpha\beta} \otimes \boldsymbol{a}^{\alpha\beta}\right), \qquad [\![\boldsymbol{\sigma}]\!]^{\alpha\beta}\boldsymbol{n}^{\alpha\beta} = \boldsymbol{0}, \tag{8}$$

where $[\![\psi]\!]^{\alpha\beta} = \psi^\alpha - \psi^\beta$ denotes a jump across interface region and $\boldsymbol{n}^{\alpha\beta}$ is the local interface normal. Based on these equations, the effective material behavior is defined and the effective stress $\boldsymbol{\sigma}$ and an effective stiffness tensor can be calculated. Chemical expansion is incorporated via the inelastic strain

$$\boldsymbol{\varepsilon}_{\mathrm{ch}}^\alpha = \beta^\alpha(\mathrm{pO_2})\,\boldsymbol{1}, \qquad \beta^\alpha(\mathrm{pO_2}) = \frac{a^\alpha(\mathrm{pO_2}) - a^\alpha(0)}{a(0)}, \tag{9}$$

where the lattice parameter a^α depends on the local oxygen partial pressure $\mathrm{pO_2}$, as determined experimentally for the ceria-based phases. The data, used in this study, can be found in [24].

Porous phases are modeled as phases with vanishing stiffness. Applying the jump condition framework to solid-pore interfaces leads to an ill-posed momentum, since the balance of linear momentum at a singular surface reduces to $\boldsymbol{\sigma}^\alpha\boldsymbol{n}^{\alpha\mathrm{p}} = \boldsymbol{0}$. Therefore, strains are assumed to be equal in these pairwise interactions:

$$[\![\boldsymbol{\varepsilon}]\!]^{\alpha\mathrm{p}} = \boldsymbol{0}, \qquad \boldsymbol{a}^{\alpha\mathrm{p}} = \boldsymbol{0}. \tag{10}$$

This reduces the system of unknowns, which is solved in order to determine the effective material behavior.

Governing equations. Based on minimizing the free energy of the system, the evolution of the order parameters follows as superposition of pairwise interactions [25]:

$$\frac{\partial\phi^\alpha}{\partial t} = -\frac{1}{N\epsilon}\sum_{\beta\neq\alpha}^{N} M^{\alpha\beta}\left(\frac{\delta f_{\mathrm{intf}}(\nabla\boldsymbol{\phi},\boldsymbol{\phi})}{\delta\phi^\alpha} - \frac{\delta f_{\mathrm{intf}}(\nabla\boldsymbol{\phi},\boldsymbol{\phi})}{\delta\phi^\beta} + \frac{8\sqrt{\phi^\alpha\phi^\beta}}{\pi}\left([\![f_{\mathrm{el}}]\!]^{\alpha\beta} - \boldsymbol{\sigma}\cdot[\![\boldsymbol{\varepsilon}]\!]^{\alpha\beta}\right) + \Delta_{\mathrm{acurv}}^{\alpha\beta}\right), \tag{11}$$

with the mobilities $M^{\alpha\beta}$ and the variational derivative

$$\frac{\delta f_{\mathrm{intf}}}{\delta\phi^\alpha} = \frac{\partial f_{\mathrm{intf}}}{\partial\phi^\alpha} - \nabla\cdot\frac{\partial f_{\mathrm{intf}}}{\partial\nabla\phi^\alpha}. \tag{12}$$

For the derivative of the contribution from the strain energy, the reader is referred to [26,27]. Furthermore, $\Delta_{\mathrm{acurv}}^{\alpha\beta}$ is an additional non-variational driving force that decouples physical and numerical interfacial energies [28] and enables calibration of curvature-driven interface evolution by a surface energy γ^{c}, which does not contribute

to curvature minimization. Variation of the free energy with respect to the displacement yields the equilibrium equation for mechanical equilibrium under quasi-static conditions and neglected body forces

$$\mathrm{div}(\boldsymbol{\sigma}) = \mathbf{0}. \tag{13}$$

2.5. Generation of virtual microstructures

To investigate the mechanical response of varying SOEC microstructures, we employ a physics-informed virtual microstructure generator originally developed for multilayer SOFCs, as described by Schöller et al. [12]. The generator constructs three-dimensional microstructures with controlled morphology using discrete-element particle packing, graph-based connectivity modeling, and spherical-harmonics particle-shape reconstruction. After shape generation, the structures are voxelized and embedded into a multiphase-field representation that is fully compatible with the electro-chemo-mechanical framework used here. All simulations are carried out with the parallel phase-field code PACE3D [29]. Within this framework, systematic variations of microstructural features, such as particle size, porosity, and layer thickness, can be studied independently of experimental constraints. In the following, the individual steps are described briefly. For an extensive introduction, the reader is referred to [12].

Discrete-element packing of spheres. The generator workflow starts by constructing a dense packing of spherical particles using a discrete element method (DEM). The DEM formulation explicitly resolves interparticle repulsive contact forces, viscous damping, and constraints across the layer boundaries, enabling realistic packing of polydisperse spheres across SOEC layers. This procedure yields an equilibrated configuration in which prescribed particle-size distributions, layer-resolved material compositions, and target volume fractions are reproduced.

Neighbor-graph and contact constraints. From the final DEM packing, a neighbor graph is constructed using a modified minimum-spanning-tree (MST) graph. The MST ensures global connectivity, while additional edges are inserted between particles whose free surface distances fall below prescribed thresholds. This extended graph captures the contact topology and enables physically meaningful interparticle connectivity without over-constraining the system. For each pair of connected particles, a geometric contact point is computed from their radii-weighted center positions. These contact relations later act as geometric constraints during particle-shape reconstruction, ensuring that the generated microstructure exhibits features consistent with experimentally observed SOFC microstructures.

Particle-shape construction via spherical harmonics. The particle shapes are then constructed by modeling a local varying fluctuation of the particle radii in terms of real spherical harmonics up to a maximum angular degree. The angular power spectrum controls the surface complexity of the particles and provides statistical tuning of morphological features such as roughness, anisotropy, and deviation from sphericity. The spherical-harmonics coefficients are sampled from distributions governed by the target power spectrum but are further constrained so that the reconstructed surface satisfies all neighbor-graph contact points. This yields irregular particle shapes whose morphology matches experimentally reconstructed SOFC particles (e.g., from FIB-SEM data), while ensuring physically consistent interparticle contact.

Voxelization and multiphase-field representation. After the particle shapes have been generated, the geometry is voxelized on a regular Cartesian grid and embedded in a multiphase-field description that is directly compatible with the electro-chemo-mechanical framework used in this work. All simulations are performed with the structured-grid phase-field framework PACE3D [29], which provides a mature environment for large-scale 3D microstructure calculations. PACE3D combines optimized stencil-based numerics with MPI-parallel domain decomposition and dynamic load balancing, enabling efficient simulations on massively parallel hardware. Within this environment, the Local Reduced Order Parameter (LROP) [30,31] strategy is employed to activate phase fields only where the corresponding particles occur locally, allowing hundreds to thousands of particles to be treated efficiently without sacrificing accuracy. The same software framework has been used in a broad range of applications, including grain growth and coarsening, sintering, solidification, martensitic transformations, multiphase flow, and mechanically coupled phase-field models [31]. In the present study, the resulting diffuse-interface representation provides a scalable and robust basis for resolving the virtual SOEC microstructures in fully coupled electro-chemo-mechanical simulations.

Morphological accuracy and calibration. The generator workflow is able to reproduce both porous and dense SOFC layers by input parameters, such as particle size distributions, layer-specific target porosities, angular power spectra for particle shapes and post-voxelization morphological dilation. In its original formulation, the generator was calibrated through a multi-objective Bayesian optimization loop, matching experimentally reconstructed microstructures in terms of volume fraction, tortuosity, specific surface area, and equivalent radius distributions. The main objective of this study is to investigate the mechanical behavior of microstructure variations that go beyond what is feasible in experiments, while maintaining physical realism in terms of particle connectivity, interface geometry and porosity distribution. Therefore, calibration of certain morphological quantities, such as equivalent radius distributions, has been omitted as they are not expected to be sensitive to the overall mechanical behavior. See Section 3.1 for details about the generated microstructures.

Sintering-like morphologies via MPFM. In SOECs, sintering and operational aging continuously changes the microstructure, altering for example tortuosities, specific surface areas, and triple-phase boundary lengths. The structure generation workflow so far is based on particle packing and, by construction, does not enforce interfacial curvature or surface-energy minimization. In contrast, real microstructures evolve toward lower-energy configurations during sintering and cell operation. Fully physical-based simulations of these processes, incorporating mass transport, interfacial thermodynamics, and coupled chemo-mechanics, are nontrivial and beyond the scope of this work. Instead, we employ the MPFM to evolve the initially packed microstructure via curvature-driven interfacial forces and energy minimization to achieve a sintering-like morphological coalescence in the virtual microstructures. This is achieved by employing the modified classical Allen-Cahn phase-field equation with the volume-preserving approach [32] and a correction [28], enabling the calibration of the curvature-minimizing dynamics by a surface energy γ^c term. The qualitative outcomes of this evolution results are presented in Section 3.1. A quantitative evaluation of the MPFM aging step is not performed in this work, instead the reader is referred to [33] for a recent extensive study of such approach applied to SOFC microstructures.

2.6. Distribution of oxygen partial pressure

The distribution of the oxygen partial pressure pO_2 across the layered cell architecture follows from the electrochemical boundary conditions at the electrodes and from the transport behavior within the electrolyte and fuel electrode. The formulation builds on the work of Riess [34], Gödickemeier and Gauckler [35], Dierickx et al. [36] and the recent analysis by Lenser et al. [11].

The treatment of the GDC/YSZ/GDC electrolyte stack as an effective electrolyte is a simplifying assumption of the present model. A more accurate description would require a layer-resolved electrochemical transport model including the YSZ blocking layer, the GDC layers, and possible GDC-YSZ interdiffusion regions. Such approaches have been reported for GDC-YSZ electrolyte systems and show that the oxygen-potential drop can be strongly localized near the GDC/YSZ

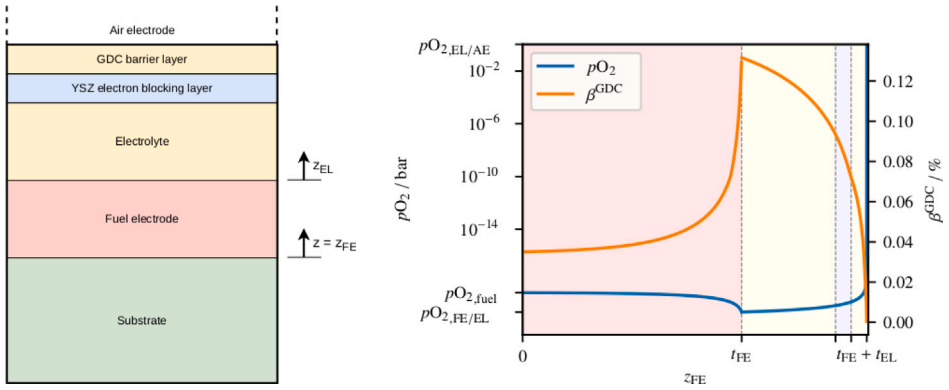

(a) Structure of the cell. (b) pO_2 and chemical expansion distribution.

Fig. 2. (a) Structure of the multilayered cell with the corresponding layer coordinates. (b) Exemplary distribution of the oxygen partial pressure pO_2 and chemical expansion β^{GDC} across the cell, excluding the substrate and air electrode layers.

interface or within interfacial regions [37]. In the present study, the pO_2 profile is used as a prescribed electrochemical loading condition for the microstructure-resolved mechanical model. The resulting stress magnitudes should therefore be interpreted as values obtained under this defined electrochemical loading assumption.

At the air electrode, the surrounding atmosphere is assumed to consist of 21 % O_2 and 79 % N_2. At 1 bar ambient pressure, this yields the oxygen partial pressure of $pO_{2,air} = 0.21$ bar. The oxygen partial pressure on the fuel side is obtained from the Nernst equation, using the open-circuit voltage $V_{OC} > 0$, interpreted as the reference cell voltage at zero current density,

$$pO_{2,fuel} = pO_{2,air} \exp\left(-\frac{4F}{RT} V_{OC}\right), \tag{14}$$

with the universal gas constant R, the Faraday constant F and the absolute temperature T. Similarly, the partial oxygen pressure at the interface between the electrolyte and air electrode (AE) and fuel electrode (FE) can be calculated by

$$pO_{2,EL/AE} = pO_{2,air} \exp\left(\frac{4F}{RT} \eta_{AE}\right), \tag{15}$$

$$pO_{2,FE/EL} = pO_{2,fuel} \exp\left(\frac{4F}{RT} \eta_{FE}\right), \tag{16}$$

with the overpotentials η_{AE}, η_{FE} of the air and fuel electrode. The distribution of the oxygen partial pressure in the electrolyte, from $pO_{2,FE/EL}$ to $pO_{2,EL/AE}$ is modeled by

$$pO_{2,EL}(x_{EL}) = pO_{2,FE/EL}\left(1 - \frac{1 - \exp\left(-\frac{e}{k_B T} \Delta V \frac{z_{EL}}{t_{EL}}\right)}{1 - \exp\left(-\frac{e}{k_B T} \Delta V\right)} \left(1 - \frac{pO_{2,FE/EL}}{pO_{2,EL/AE}}\right)\right)^{-1}, \tag{17}$$

with elementary charge e, the Boltzmann constant k_B, the thickness of the electrolyte layer t_{EL} (including the thickness of the YSZ and GDC barrier layers) and the coordinate along the layer z_{EL} with its origin at the fuel electrode interface. The voltage difference ΔV is assumed to be

$$\Delta V = V_{OC} - V_{MC}, \tag{18}$$

with the voltage of the mixed conductor $V_{MC} = V_{cell} - \eta_{FE} - \eta_{AE}$, which defines the qualitative distribution of oxygen partial pressure in the layer. The lowest partial pressure at the starting interface is defined by $pO_{2,FE/EL}$, and the increase of pressure over the electrolyte layer is defined by $(1 - pO_{2,FE/EL}/pO_{2,EL/AE})$. Based on the work of Dierickx et al. [36], the oxygen partial pressure distribution in the fuel electrode is modeled by

Table 2
Mechanical material properties of each material with their corresponding references.

Property	GDC	YSZ	Ni
Young's modulus in GPa	152 [38]	143 [38]	169 [39]
Poisson ratio	0.28 [40]	0.41 [40]	0.31 [41]
Chemical expansion	see [24]	0	0

$$pO_{2,FE}(x_{FE}) = pO_{2,fuel} + \left(pO_{2,FE/EL} - pO_{2,fuel}\right) \exp\left(\frac{z_{FE} - t_{FE}}{\lambda}\right), \tag{19}$$

where t_{FE} is the thickness of the FE layer and z_{FE} the coordinate along the layer with its origin at the substrate interface. The penetration depth λ is set to 2 µm according to [11].

Oxygen partial pressure pO_2 across the cell is governed by electrode boundary conditions and transport: The Nernst equation and electrode overpotentials set interfacial pO_2. Within the electrolyte, pO_2 increases steeply due to the internal potential drop ΔV, and in the fuel electrode it relaxes with the penetration depth λ, yielding a continuous profile, as illustrated in Fig. 2(b).

3. Results

All simulations represent an SOEC operating at 750 °C with a fixed current density of 1.5 A cm^{-2}. The material parameters used in the model are summarized in Table 2, and the electro-chemical properties are listed in Table 1. Section 3.1 briefly outlines the generation of the microstructures, which are based on a reconstruction of an experimentally manufactured SOEC cell and subsequently reproduced using the virtual microstructure generator. Section 3.2 introduces the applied mechanical boundary conditions and motivates the use of an effective in-plane strain to represent the mechanical constraints imposed by the cell environment. In the remaining subsections, we examine the resulting stress distributions for systematic variations in layer size, porosity, and overpotential, highlighting the influence of each parameter on the electro-chemo-mechanical response.

3.1. Generation of virtual microstructures

The microstructures are based on a three-dimensional reconstruction of a fully screen-printed experimental SOEC cell, shown in Fig. 3a. The reconstruction was used to extract representative morphological descriptors for the virtual microstructure generator. The generated structures are therefore morphology-controlled model systems derived from experimental descriptors, but they are not intended as direct replicas of a specific manufacturing route.

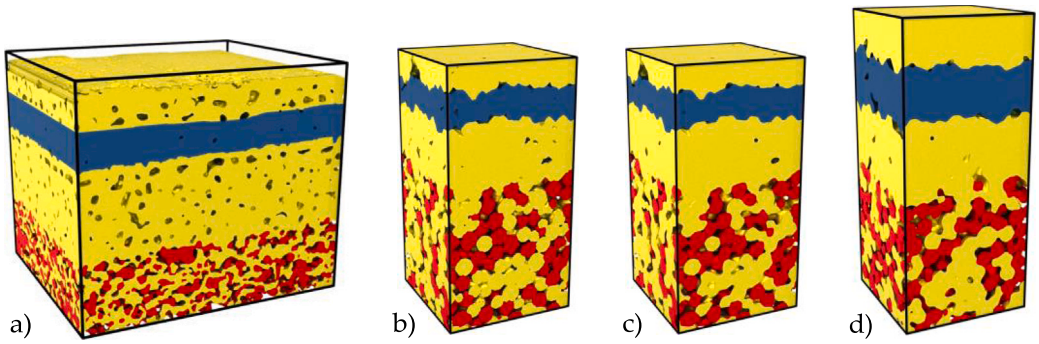

Fig. 3. (a) Microstructure reconstruction of a fully screen-printed experimental SOEC. Virtual microstructure with similar morphological properties after the generation (b), after aging simulation based on the MPFM (c), and with varying layer thicknesses (d). The red phase represents Ni, the yellow phase GDC, and the blue phase YSZ. (For interpretation of the references to color in this figure legend, the reader is referred to the web version of this article.)

The reconstructed volume measures approximately 29 µm × 25 µm × 25 µm at a spatial resolution of ≈33 nm, and contains the four layers relevant for this study: The fuel electrode (FE), the electrolyte (EL), the YSZ electron blocking layer, and the GDC barrier layer, with thicknesses of 8, 8.5, 3 and 3 µm, respectively.

For the numerical simulations, virtual microstructures were generated with an in-plane base size of 200 × 200 elements and the same spatial resolution of 33 nm, consistent with the experimental dataset. The virtual microstructure generator was calibrated using quantitative descriptors extracted from the reconstruction. Specifically, we targeted the experimentally determined volume fractions (FE: 31.12 % Ni, 48.79 % GDC; EL: 92.26 % density; YSZ electron blocking layer: 92.26 % density; GDC barrier layer: 86.97 % density), tortuosities (FE: 7.30 for Ni, 2.26 for GDC; EL: 1.06; GDC barrier: 1.10), and specific surface areas in the FE (0.236 nm^{-1} for Ni and 0.155 nm^{-1} for GDC).

The applied optimization workflow described in [12] achieved accuracy across all layers. In the FE, the largest deviation occurred in the tortuosity values (≈5 %), with all other metrics within 0.35–2.30 % of the target. Deviations in the remaining layers were similarly small (EL volume fraction 2.63 % and tortuosity 0.81 %; YSZ electron blocking layer volume fraction 0.003 %). For the GDC barrier layer, the contrast in low tortuosity and higher porosity leads to relatively higher errors with 5.29 % for the volume fraction and 1.63 % for the tortuosity. A representative calibrated microstructure is shown in Fig. 3b, featuring layer thicknesses of 7 µm (FE), 3 µm (EL), 1.5 µm (YSZ barrier) and 1.5 µm (GDC barrier). Subsequently, aging of the SOEC structure was simulated based on the MPFM using $M = 1\,\mathrm{s\,nm^2\,kg^{-1}}$, $\epsilon = 4\Delta x/\pi^2$, and interface energies $\gamma^{\mathrm{p,Ni}} = 1.2\,\mathrm{kg\,s^{-2}}$, $\gamma^{\mathrm{p,GDC}} = \gamma^{\mathrm{p,YSZ}} = 2\gamma^{\mathrm{p,Ni}}$, $\gamma^{\mathrm{GDC,YSZ}} = 1.0\,\mathrm{kg\,s^{-2}}$, and $\gamma^{\mathrm{c}} = 450\,\mathrm{kg\,s^{-2}}$. A simulation time of 250 s was used for all aging runs. An example of the resulting morphology is shown in Fig. 3c.

Finally, the calibrated structures were systematically modified to study how morphology influences the mechanical response. The objective of this study is not to reproduce specific manufacturing processes, but rather to explore the effects of controlled changes on electro-chemo-mechanical stresses. This involves modifying the thicknesses of the GDC and YSZ layers to emulate the influence of different manufacturing routes, such as PVD for layers with submicron thickness and screen-printing for layers in the µm-range, as well as increasing the YSZ electron blocking layer thickness, and varying the fuel-electrode overpotential to represent degraded electrochemical performance. Fig. 3d shows an example of a modified structure with increased barrier-layer thicknesses.

In the following parameter studies, the thickness of the fuel-side GDC layer is kept fixed. The varied GDC thickness refers to the air-side GDC barrier layer. This terminology is used to distinguish the position and function of the individual layers within the GDC/YSZ/GDC electrolyte stack; it does not imply that the layers are electrochemically independent. The choice of varied layers follows the experimental design question addressed here, namely the transition from thin PVD-derived YSZ/GDC barrier layers to thicker screen-printed barrier layers, while the fuel-side GDC layer is already screen-printed in the considered cell architecture.

3.2. Boundary conditions

To evaluate the effective electro-chemo-mechanical response of the virtual microstructures, appropriate mechanical boundary conditions are applied. The microstructures represent periodic sections of the functional layers and are therefore subjected to in-plane periodicity. Along the z-axis, the lower boundary is fixed in orthogonal displacement, while the upper boundary is stress-free

$$u_z(z=0) = 0, \qquad \boldsymbol{\sigma n}\Big|_{z=L} = \mathbf{0}. \tag{20}$$

The lateral boundaries follow periodic conditions of the form

$$\boldsymbol{u}^{+} = \boldsymbol{u}^{-} + \hat{\boldsymbol{u}}_i, \qquad \text{with } \hat{\boldsymbol{u}}_x = \hat{\varepsilon} L_x \boldsymbol{e}_x, \qquad \hat{\boldsymbol{u}}_y = \hat{\varepsilon} L_y \boldsymbol{e}_y, \tag{21}$$

with the displacement $\boldsymbol{u}^{\pm}$ at opposite lateral faces and with the corresponding $\hat{\boldsymbol{u}}_i$ at each lateral direction. $\hat{\varepsilon}$ denotes the imposed effective in-plane strain. It should be noted that the effective in-plane strain $\hat{\varepsilon}$ is not imposed at the lower boundary. The lower boundary is fixed only in the out-of-plane displacement to remove rigid-body motion and to represent the support by the substrate. The in-plane constraint is prescribed through the lateral periodic boundary conditions. Thus, $\hat{\varepsilon}$ represents the average in-plane expansion state of the functional-layer RVE. This effective strain controls the degree to which the microstructure is able to expand in response to chemically induced eigenstrains. Different choices of $\hat{\varepsilon}$ therefore lead to different effective stress states. The effective in-plane stress is evaluated by

$$\hat{\sigma} = \frac{1}{2}\left(\langle \sigma_{xx} \rangle + \langle \sigma_{yy} \rangle\right), \qquad \text{with } \langle \psi \rangle = \frac{1}{V}\int_V \psi \, dv. \tag{22}$$

representing the volume-averaged normal stresses in the directions of periodicity.

Choice of effective strain. Fig. 4 shows the resulting stress–strain response obtained by imposing various effective strains on the microstructure based on the reconstructed structure with the layer thicknesses of 7 µm (FE), 3 µm (EL), 1.5 µm (YSZ electron blocking layer) and 1.5 µm (GDC barrier layer), as shown in Fig. 3c. The microstructure exhibits a linear relationship between the effective stress $\hat{\sigma}$ and the effective strain $\hat{\varepsilon}$, with the slope corresponding to the effective in-plane Young's modulus, where a linear fit yields 144 GPa. At zero applied strain ($\hat{\varepsilon} = 0$), the chemically expanding materials are constrained by the surrounding layers, generating a compressive effective normal stress. Conversely, the strain at which $\hat{\sigma} = 0$ holds corresponds to the effective chemical expansion of the microstructure with 0.057 %.

To represent the experimental situation, including the mechanical support of the substrate, the classical laminate theory [42] was used

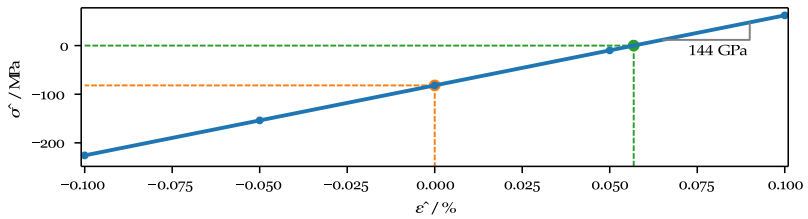

Fig. 4. The stress–strain curve of the imposed effective in-plane strain $\hat{\varepsilon}$ versus the effective in-plane normal stress $\hat{\sigma}$. The system exhibits linear behavior with an effective Young's modulus and an intercept that can be interpreted as an effective inelastic strain.

to estimate the constrained expansion of the functional layer bonded to a thick substrate. The 450 µm thick substrate layer is assumed to be isotropic with a Young's modulus of 23.8 GPa [43]. For the 11 µm thick isotropic functional layer, the Young's modulus and eigenstrain are based on the previous calculations. The Poisson ratio for both layers is set to 0.28 [44]. For the calculation of the resulting values, the software eLamX^2 [45] was used. Assuming no forces and moments, the mean expansion of the whole system is small (≈0.0056 %) due to the strong mechanical support of the substrate. In contrast, the expansion in only the functional layer is approximately 0.02 % leading to a stress in this layer of −70 MPa. Moreover, the curvature of the whole system is negligible with 7.12×10^{-7} µm^{-1}.

The value $\hat{\varepsilon} = 0.02\,\%$ does not correspond to the free chemical expansion of the functional layers. The zero-stress condition in Fig. 4 gives an effective unconstrained chemical expansion of approximately 0.057%. In contrast, the value 0.02 % represents the partially constrained expansion of the functional layers when bonded to the thick substrate, as estimated by classical laminate theory. The smaller global expansion of the complete substrate/functional-layer system, approximately 0.0056 % is dominated by the 450 µm thick substrate and therefore does not directly represent the average strain state of the microstructurally resolved functional-layer volume element. Thus, the applied boundary condition represents a partially constrained supported-cell state, not a fully clamped condition.

The mechanical constraint at stack level is decisive for the absolute stress state in the cell. Depending on sealant geometry, interconnect thickness, external clamping, and possible creep relaxation, the cell may experience different constraint states, ranging from nearly free deformation to strongly constrained in-plane expansion [11]. Therefore, there is no unique boundary condition that represents all possible stack configurations. In the present work, the imposed effective strain is used to define a representative partially constrained state of the functional layers, allowing the local microstructural stress concentrations to be evaluated under a prescribed mechanical constraint.

An explicit substrate representation was not included because a fully resolved microstructure-scale simulation of the 450 µm thick support together with the approximately 11 µm thick functional layers at the voxel resolution of 33 nm is computationally infeasible.

Since the virtual microstructures do not include the substrate, the effective strain is imposed via the boundary condition by setting $\hat{\varepsilon} = 0.02\,\%$ in the following sections to recover the appropriate compressive stress state in the functional layers. This approach retains the relevant large-scale mechanical constraint imposed by the support while keeping the simulations focused on the local electro-chemo-mechanical stress concentrations in the microstructurally resolved functional layers.

3.3. Stress distribution

In this subsection, the general stress distribution of the introduced SOEC microstructures will be investigated. Therefore, the microstructure and mechanical boundary conditions from Sections 3.1 and 3.2 are used. The full three-dimensional stress field is evaluated to assess the mechanical response. Since stresses are tensorial quantities, different quantities can be extracted depending on the mechanical question, including individual stress components, directional normal stresses, or scalar stress measures. In the present work, the maximum normal stress (largest absolute principal stress) according to Rankine theory is used as the primary scalar stress measure. This choice is motivated by the brittle character of the ceramic electrolyte and barrier layers, for which local normal stress concentrations are relevant for crack initiation. Directional stresses, such as the effective in-plane normal stress introduced in Section 3.2, characterize the global constraint state, but do not generally represent the locally critical stress state near pores, interfaces, and material junctions. Fig. 5(a) illustrates the resulting maximum normal stress field across the domain. The highest stresses occur within the electrolyte layer where the GDC exhibits chemical expansion, and distinct stress concentrations appear at pores and material interfaces due to geometrical features and material contrasts. To clarify the tensorial stress state underlying this scalar stress measure, additional signed stress statistics for the reference microstructure are provided in Fig. S1 of the Supplementary Material. These include the mean in-plane normal stress, the out-of-plane normal stress, and the maximum and minimum principal stresses. The absolute stress scale for the reference microstructure is given in Fig. 5. In the subsequent parameter studies, the same stress measure is reported in normalized form to compare relative changes caused by variations in layer thickness, porosity, or overpotential.

Because direct interpretation of the full-field stress distribution is challenging, the data is reduced to allow a comprehensible overview of the distribution along the cell stacking direction. Fig. 5(b) shows stress quantiles as a function of the microstructure height. The highest median local stresses occur within the electrolyte, but the GDC barrier layer also experiences elevated stresses. At the lower quantiles, the stresses remain small, indicating always practically stress-free regions. This is likely due to the porous character of the microstructure. At higher quantiles, including the maximum local stress, pronounced peaks are observed at boundaries toward other layers, especially within the electrolyte layer. These stress concentrations result from the superposition of chemical eigenstrain due to local oxygen partial pressure and the mismatch in mechanical properties across solid–solid interfaces, further amplified by the changes in porosity. The locations of these peak stresses indicate mechanically critical regions and potential sites for crack initiation. In the YSZ blocking layer, the stress field is not spatially uniform. Instead, the height-resolved statistics indicate that the mechanically critical values occur close to the adjacent GDC/YSZ interfaces, where chemical eigenstrains in the neighboring GDC layers, elastic mismatch, and local interface geometry interact. Consequently, the model can identify mechanically critical regions in and near the YSZ layer, but it cannot determine whether a crack will actually nucleate without an additional fracture criterion. The signed stress state underlying this interpretation is further illustrated in Fig. S1 of the Supplementary Material.

Previous post-test analysis of the same ceria-based SOEC architecture showed electrolyte cracking after operation at high electrolysis current density [11]. The present model cannot directly predict crack formation, because it does not include an explicit fracture criterion, flaw-size distribution, subcritical crack growth, or crack-propagation model. A direct simulation of crack initiation and propagation would

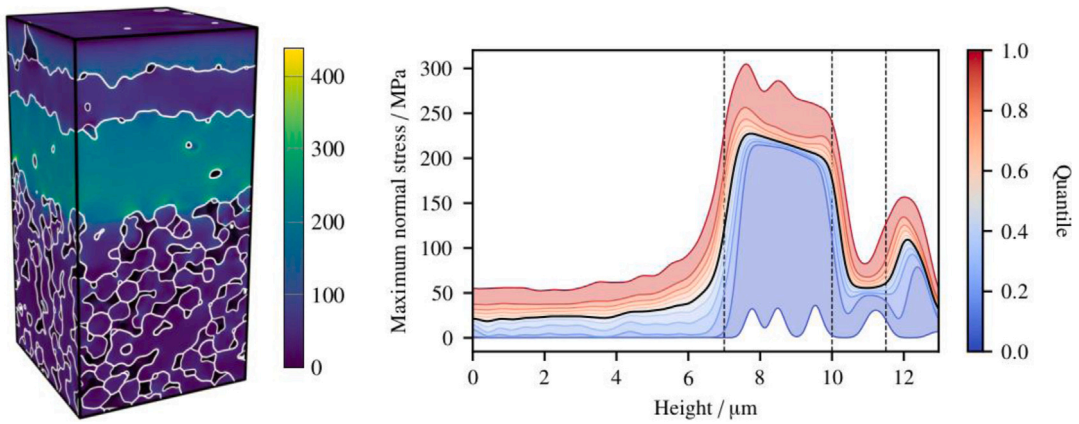

(a) Full field distribution. (b) Statistical distribution over height.

Fig. 5. Exemplary maximum normal stress. (a) A full three-dimensional stress distribution with white contour lines between the different materials. (b) The statistical distribution of these stresses over the height of the microstructure for different quantiles, with the median highlighted in black. The vertical dotted lines indicate the layer interfaces. (For interpretation of the references to color in this figure legend, the reader is referred to the web version of this article.)

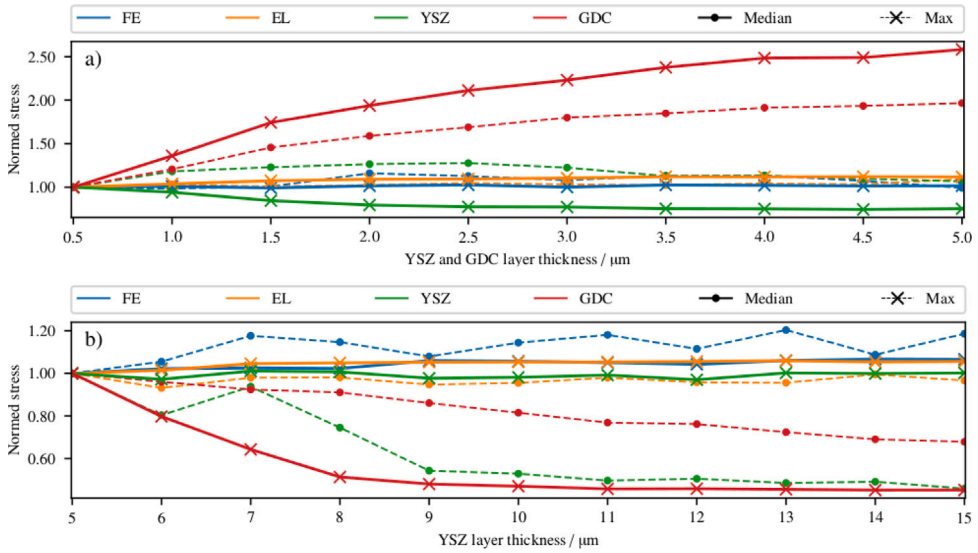

Fig. 6. The relative change of the median and maximum of the maximum normal stress for different layer thicknesses of the YSZ and GDC barrier layer (a) and a further increase of the YSZ electron blocking layer thickness (b). The stresses are therefore normalized by the value for the thinnest layers.

require an additional fracture-mechanical formulation, for example a phase-field fracture approach as used in Schöller et al. [46]. The spatially resolved stress field in Fig. 5 is nevertheless consistent with the experimentally observed failure mode, since elevated maximum normal stresses occur in the electrolyte and near the adjacent GDC/YSZ interfaces. These stress concentrations identify mechanically critical regions of the cell and provide a qualitative indication of where failure may be promoted under electro-chemo-mechanical loading. Consequently, the following parameter studies are interpreted primarily with respect to their influence on these critical stress concentrations, rather than as deterministic predictions of crack initiation or crack propagation.

3.4. Variation of GDC & YSZ barrier layer thickness

This subsection investigates the influence of the YSZ electron-blocking layer and the air-side GDC barrier layer thickness on the stress state, while the fuel-side GDC layer thickness is kept fixed at the reference value extracted from the screen-printed reconstruction. This parameter choice reflects the focus of the present study: the mechanical consequences of changing from a PVD-based cell architecture with thin YSZ/GDC barrier layers to a screen-printed architecture with thicker barrier layers. The fuel-side GDC layer is not considered less relevant; however, its thickness is kept fixed because it is not the primary manufacturing variable in the transition studied here. Varying this layer would address an additional design question concerning the complete electrolyte stack and is therefore left for future work.

All other aspects of the microstructure generation, and mechanical boundary conditions, follow Sections 3.1 and 3.2. To enable a comprehensible comparison of stress behavior across different microstructures, the information of such simulations, see Section 3.3, is reduced to layer-averaged metrics. Specifically, each case is summarized by the median of the maximum normal stress, which characterizes the typical level of the chosen Rankine-type stress measure in a brittle layer, and the peak value of the maximum normal stress, which captures local stress concentrations relevant for damage initiation. The stresses in the following parameter studies are normalized by the respective reference case. This normalization is used deliberately to emphasize relative trends between microstructural variants, whereas the absolute stress scale of the reference microstructure is shown in Fig. 5 and Fig. S1 of the Supplementary Material

Fig. 6a presents the layer-averaged median and maximum stress for each layer for simulations with systematically varied GDC and YSZ barrier layer thicknesses. To make the results directly comparable, all stresses are normalized by the values obtained for the thinnest layers. Consequently, each curve starts at 1.0, and deviations indicate the relative change with increasing layer thickness with respect to this reference. The fuel electrode (FE) shows no dependence on layer thickness, as the chemical strains remain unchanged, and the layer is not adjacent to any barrier layer. The electrolyte (EL), despite adjacency to the YSZ layer, does not exhibit a consistent trend with increasing layer thickness. Distinct trends were observed within the barrier layers. For the YSZ electron blocking layer positioned between two GDC layers, increasing thickness reduces stress. A thicker YSZ layer results in a more uniform redistribution of the load caused by chemical strains in neighboring ceria. This lowers the characteristic stresses within the YSZ electron blocking layer. On the other hand, the GDC barrier layer showed a clear increase in stress for thicker layers, with the median rising more than the maximum. This behavior is dominated by the lower local oxygen partial pressure reached in a thicker GDC barrier compared with thin layers, where pO_2 remains closer to the air-electrode value. The lower local oxygen partial pressure corresponds to a stronger reduction of ceria and therefore increases the local chemical expansion, which elevates the stress level in the GDC barrier layer.

The interpretation of the barrier-layer stresses depends on the prescribed pO_2 profile. The dominant chemical-expansion contribution is expected in the fuel-side GDC layer adjacent to the Ni–GDC electrode, where GDC is strongly reduced and exhibits mixed conduction. A refined treatment of the YSZ blocking layer and possible interdiffusion regions would mainly affect the detailed pO_2 distribution near the GDC/YSZ interfaces and in the air-side GDC barrier layer. Therefore, such a treatment would improve the quantitative accuracy of the calculated stress magnitudes, but it is not expected to alter the main purpose of the present parameter studies, namely the identification of systematic mechanical trends under a prescribed electrochemical loading state.

Previous analysis of ceria-based SOECs suggested that electro-chemo-mechanically induced stresses in the YSZ blocking layer and adjacent interfaces can contribute to mechanical failure [11]. The present spatially resolved simulations support this interpretation by showing elevated maximum-normal-stress values near the GDC/YSZ interfaces. These stress concentrations indicate mechanically critical regions and possible crack-initiation sites. However, because the present model does not include an explicit fracture criterion or crack-propagation model, the calculated stresses should not be interpreted as a deterministic prediction of crack formation.

3.5. Variation of YSZ barrier layer thickness

Starting with the thickest barrier layer configuration of 5 μm, only the YSZ electron blocking layer thickness is increased further while keeping the GDC barrier thickness fixed. This is motivated by the experimental finding that 5 μm thickness of YSZ is insufficient to yield a fully electron-blocking layer in a co-fired cell, which will be described in detail in a forthcoming publication.

The relative changes in median and maximum stress per layer are summarized in Fig. 6b. Across the variation, the fuel electrode and the electrolyte layer exhibit no distinct change in either median or maximum of the maximum normal stress, indicating that the mechanical response is localized to the barrier layer regions. In the YSZ electron blocking layer, the median of the maximum normal stress remains essentially constant as the layer becomes thicker. In contrast, the GDC barrier layer shows a reduction in median stress that is approximately linear up to a YSZ thickness of about 8 μm, beyond which the median approaches a nearly constant value. This is likely due to the scaling of the oxygen partial pressure profile across the cell for thicker YSZ electron blocking layers; increasing the effective layer shifts the steep rise in pO_2 further into the GDC barrier and lowers the local pO_2 in the now relatively thinner GDC layer. The resulting reduction in chemical expansion diminishes the maximum normal stress in GDC and reduces stress concentrations overall. Both barrier layers exhibit a similar, monotonic decrease in maximum stress with increasing YSZ thickness, pointing to the YSZ/GDC interface as the primary origin of peak stress. The decrease of maxima with thicker YSZ is consistent with the shifted pO_2 gradient, which together reduce interfacial stress concentrations.

This analysis suggests that for the given GDC thicknesses, a YSZ thickness of more than 8 μm does not yield a reduction in mechanical stress, while increasing cell resistance. These calculations provide a guide to cell design, although it must be stressed that the presented results emphasize the relative changes over accuracy in absolute values.

3.6. Variation of GDC & YSZ barrier layer porosity

In contrast to changing the layer thickness, the porosity of the barrier layers can be varied while keeping layer sizes constant. To isolate porosity effects, both barrier layers were fixed at 5 μm thickness, and only their porosity was modified. This reflects the influence of the manufacturing methods on the resulting microstructures, where methods such as PVD lead to highly dense layers, while the porosity of a co-sintered, three-layer electrolyte is highly dependent on the absolute and relative shrinkage rates of the individual layers, their thickness, their dynamic viscosity as well as sintering time and heating rate. A controlled, experimental variation of the porosity is therefore extremely challenging. The elaboration of synthetic microstructures allows for a systematic evaluation of the influence of porosity. Because the virtual microstructures are generated from random seeds, the realized porosities vary stochastically around their targets, and the evaluated stresses are sensitive to these variations. Therefore, to obtain robust trends transition from individual samples to an ensemble-based analysis is made. Fig. 7b summarizes the distribution of realized porosities across the generated virtual microstructures. The dataset is binned by porosity using variable bin widths but a constant number of samples per bin (nine) to ensure comparable statistical confidence across the porosity range. For each bin, the ensemble-average porosity and the corresponding ensemble-averaged layer stresses are computed. Fig. 7a displays the relative median and maximum of the maximum normal stress per layer for these ensembles, plotted against the ensemble-average porosity of each bin. Consistent with the thickness-variation study, the fuel electrode and the electrolyte show no distinct, systematic changes in either median or maximum stress over the investigated porosity range. In contrast, both barrier layers exhibit a clear trend in the ensemble-average response. The median stress decreases with increasing porosity; higher porosity reduces the effective stiffness of the barrier layers. Since loading is driven by chemical strain rather than external traction, a more compliant microstructure can accommodate imposed strain more easily, thereby reducing median stress. Moreover, the maximum stress in the GDC barrier layer shows a slight increase with porosity. This increase is attributed to the higher local stress concentrations around pores and phase boundaries that occur as the microstructure becomes more porous. Increased porosity amplifies these local heterogeneities, which explains the modest rise in peak stress despite the overall reduction in median stress.

Overall, the sensitivity of the normalized stresses to porosity is comparatively low, with relative values ranging approximately from 0.9 to 1.12 across the studied porosities, whereas previous layer-thickness studies have reported substantially larger ranges (about 0.5 to 2.6).

3.7. Variation of fuel electrode overpotential

In addition to the morphological studies, the sensitivity of mechanical response to varying the fuel-electrode overpotential η_{FE} is investigated. While the change in η_{FE} physically refers to a change in

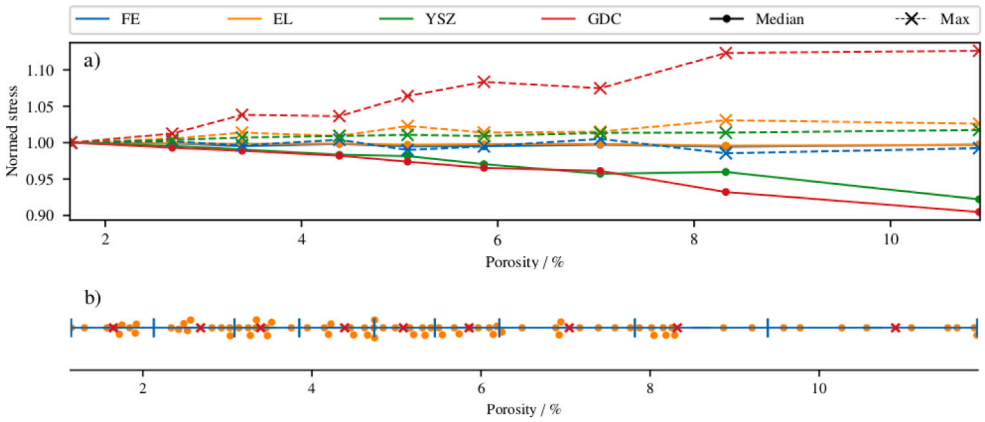

Fig. 7. The relative change in median and maximum of the maximum normal stress for different porosities of the YSZ and GDC barrier layer (a). The stresses are therefore normalized by the value for the lowest porosity. (b) Distribution of porosities for different generated microstructures (orange), the bins (blue), and mean value (red) used to calculate the averaged stresses shown in (a). (For interpretation of the references to color in this figure legend, the reader is referred to the web version of this article.)

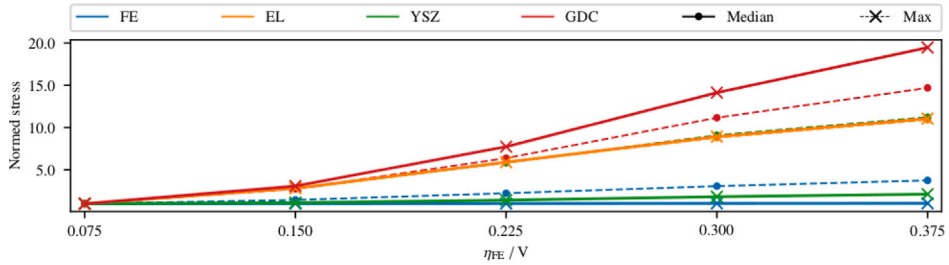

Fig. 8. The relative change of the median and maximum of the maximum normal stress for different fuel electrode overpotentials. The stresses are therefore normalized by the value for the lowest overpotential.

the microstructure of the fuel electrode, our model does not compute η_{FE} from the microstructure; therefore, it can be varied independently. The impact of microstructural changes on mechanical stresses is anticipated to be small since the main source of chemical strains is the electrolyte. The increase in η_{FE} is therefore investigated in the context both, of performance degradation during operation, as well as the influence of the electrode overpotential itself.

Simulations were performed on the microstructure defined in Section 3.1, but with both barrier layers doubled to 3 µm thickness each, under the same operating conditions as the previous sections.

Fig. 8 summarizes the relative changes in median and maximum of the maximum normal stress per layer for η_{FE} in the range $\eta_{FE} = 0.075$ to 0.375 V. Varying η_{FE} has only a minor influence on the median stresses of the fuel electrode, while the maximum stress exhibits an increase. The underlying reason is that the drop in oxygen partial pressure, induced by the overpotential, and the associated chemical expansion, is confined to a limited penetration depth (modeled by the characteristic depth λ). Thus, only a local fraction of the electrode volume close to the electrolyte is strongly affected. Additionally, the porous morphology and the chemically unaffected Ni phase compensate for these local strains, preventing a shift of the median stress but allowing localized peaks to grow. The YSZ electron blocking layer likewise exhibits only a small change in the median stress. However, because it shares interfaces with GDC on both sides, this still leads to a noticeable rise in the maximum stress with increasing η_{FE}. As expected, the largest stress increases occur in the ceria-containing layers. Both GDC in the barrier and electrolyte layer show a clear rise in stress with increasing η_{FE}, driven by the stronger chemical expansion of ceria at lower pO_2. Notably, in the GDC barrier layer the increase in the maximum stress is smaller than the increase in the median, opposite to the trend in other layers. We attribute this to stress homogenization toward the air-electrode side. In the model, the air-electrode is neglected, and the boundary is treated as a free interface, which promotes a more isotropic and uniform stress state near that boundary and suppresses local peaks, consistent with the height-resolved stress statistics shown earlier (see Fig. 5(b)). These results predict that the influence of the fuel-electrode overpotential on the stress response is higher than that of the morphological variations studied (layer thickness and porosity), underscoring a stronger sensitivity to electrochemical properties. Care must be taken to minimize η_{FE}, since its impact on the electro-chemo-mechanical stresses by far exceeds those of the electrolyte microstructure. For a given material combination, the way to minimize η_{FE} is by optimizing the processing route to obtain a microstructure with increased internal surface area and optimized porosity. The lesson for cell manufacturing is that the fabrication route should prioritize the properties of the fuel electrode over that of the electrolyte.

4. Conclusion

This work utilizes virtual microstructures to perform electro-chemo-mechanical simulations of SOECs with a ceria electrolyte. The microstructures were designed to preserve a realistic contact topology and enable physically meaningful stress analyses in the microstructure of multilayered solid oxide cells. The analysis presented here uses a 3D reconstruction of a fully screen-printed SOEC as the reference for microstructural parameters, while electrochemical boundary conditions were derived from measurements on a PVD-processed cell. This combination is used as a controlled modeling framework rather than as a direct reconstruction of one specific manufactured cell. The modeling of the gradient of the oxygen partial pressure is based on literature sources; specifically, it expands on previous work that investigated this issue using a 1-dimensional approach with homogenized layers [11].

The presented microstructure–property relations showcase the potential of using virtual microstructures to predict the impact of microstructural changes on device performance. The fabrication of cells

with controlled changes in one microstructural parameter is very time-consuming at best, and impossible at worst, since many microstructural features cannot be influenced independently of others. The use of virtual microstructures can quickly delineate the most important microstructural features with regards to a specific objective, and thus provide guidance for the cell design. Secondly, the results of this work point to several design guides which can be used to improve the durability of the cells. For instance, it was shown that the overpotential of the fuel electrode is by far the most important influence on the stresses during SOEC operation, while the porosity of the electrolyte has a comparatively smaller effect. Therefore, lowering the sintering temperature, which would limit the grain growth and thus positively affect the overpotential but also negatively influence porosity, is advisable, on balance. Furthermore, it can be shown that thicker YSZ layers reduce stresses in the multilayer electrolyte. In practice, this will have a tradeoff with increased cell resistance, so an optimum thickness for the YSZ layer can be approximated around 8 µm.

Future work should address a fully layer-resolved electrochemical treatment of the pO_2 profile, including GDC, YSZ, and possible interdiffusion regions, as well as a systematic variation of the fuel-side GDC layer thickness. Both aspects are expected to couple mechanical stresses with electrolyte resistance, oxygen-potential distribution, and chemical expansion. In the present study, the fuel-side GDC layer was kept fixed because it is already screen-printed in the considered cell architecture, while the varied YSZ and air-side GDC barrier layers represent the experimentally relevant transition from PVD-derived to screen-printed barrier layers.

As a perspective beyond the current work, it appears feasible to combine such virtual microstructures with a 3-dimensional electrochemical model that computes quantities such as the electrode overpotential directly from the microstructure. While beyond the scope of this work, this would enable the digital design of SOECs with freely configurable microstructure.

CRediT authorship contribution statement

Lukas Schöller: Writing – review & editing, Writing – original draft, Visualization, Methodology, Investigation, Formal analysis, Conceptualization. **Luzie Wehner:** Writing – review & editing, Writing – original draft, Visualization, Methodology, Investigation, Formal analysis, Conceptualization. **Denise Ramler:** Writing – review & editing, Writing – original draft, Methodology, Investigation, Conceptualization. **Iurii Kogut:** Writing – review & editing, Writing – original draft, Investigation, Formal analysis, Conceptualization. **Stefan Kucharski:** Writing – review & editing, Methodology, Investigation. **Christian Lenser:** Writing – review & editing, Writing – original draft, Supervision, Project administration, Funding acquisition, Conceptualization. **Ravi Kumar Jeela:** Writing – review & editing, Writing – original draft, Formal analysis. **Daniel Schneider:** Writing – review & editing, Supervision, Project administration, Funding acquisition. **André Weber:** Writing – review & editing, Supervision, Project administration, Funding acquisition, Conceptualization. **Ruth Schwaiger:** Writing – review & editing, Supervision, Project administration, Funding acquisition. **Britta Nestler:** Writing – review & editing, Supervision, Project administration, Funding acquisition.

Declaration of Generative AI and AI-assisted technologies in the writing process

During the preparation of this work the authors used ChatGPT in order to improve the readability and language of the manuscript. After using this service, the authors reviewed and edited the content as needed and take full responsibility for the content of the published article.

Declaration of competing interest

The authors declare that they have no known competing financial interests or personal relationships that could have appeared to influence the work reported in this paper.

Acknowledgments

We gratefully acknowledge the funding by the German Federal Ministry for Research, Technology and Space (BMFTR) for the ElCh-Fest project (Elektro-chemo-mechanische Modellierung von Ceroxid-basierten Festoxidelektrolysezellen, grant number 03SF0641A, B and C). Daniel Schneider and Britta Nestler are grateful for the support by the MSE program, no. 43.31.01 of the Helmholtz association.

Appendix A. Supplementary data

Supplementary material related to this article can be found online at https://doi.org/10.1016/j.jpowsour.2026.241459.

Data availability

The datasets generated and analyzed during the current study were produced using the proprietary Pace3D simulation framework developed at the Karlsruhe University of Applied Sciences [29,31], and the open-source Optuna optimization framework [47]. A selected representative dataset of this work has been deposited on Zenodo [48] and publicly accessible [49]. Due to licensing restrictions, the Pace3D source code cannot be made publicly available. However, licenses can be obtained upon request. The complete dataset, and detailed analysis results, are available upon request.

References

[1] L. Rorato, Y. Shang, S. Yang, M. Hubert, K. Couturier, L. Zhang, J. Vulliet, M. Chen, J. Laurencin, Understanding the Ni migration in solid oxide cell: A coupled experimental and modeling approach, J. Electrochem. Soc. 170 (3) (2023) 034504, http://dx.doi.org/10.1149/1945-7111/acc1a3.

[2] Ángel Triviño-Peláez, D. Cademartori, M. Hubert, L. Rorato, M. Prioux, J. Laurencin, Modelling the impact of Ni migration and coarsening on the Ni-YSZ electrodes performances based on three-dimensional microstructures, Electrochim. Acta 520 (2025) 145791, http://dx.doi.org/10.1016/j.electacta.2025.145791.

[3] M. Trini, A. Hauch, S. De Angelis, X. Tong, P.V. Hendriksen, M. Chen, Comparison of microstructural evolution of fuel electrodes in solid oxide fuel cells and electrolysis cells, J. Power Sources 450 (2020) 227599, http://dx.doi.org/10.1016/j.jpowsour.2019.227599.

[4] X. Sun, P.V. Hendriksen, M.B. Mogensen, M. Chen, Degradation in solid oxide electrolysis cells during long term testing, Fuel Cells 19 (6) (2019) 740–747, http://dx.doi.org/10.1002/fuce.201900081.

[5] Q. Fang, C.E. Frey, N.H. Menzler, L. Blum, Electrochemical performance and preliminary post-mortem analysis of a solid oxide cell stack with 20,000 h of operation, J. Electrochem. Soc. 165 (2) (2018) F38–F45, http://dx.doi.org/10.1149/2.0541802jes.

[6] M. Lang, S. Raab, M.S. Lemcke, C. Bohn, M. Pysik, Long term behavior of solid oxide electrolyser (SOEC) stacks, ECS Trans. 91 (1) (2019) 2713–2725, http://dx.doi.org/10.1149/09101.2713ecst.

[7] C. Lenser, H. Jeong, Y.J. Sohn, N. Russner, O. Guillon, N.H. Menzler, Interaction of a ceria-based anode functional layer with a stabilized zirconia electrolyte: Considerations from a materials perspective, J. Am. Ceram. Soc. 101 (2) (2017) 739–748, http://dx.doi.org/10.1111/jace.15214.

[8] J. Zhang, C. Lenser, N. Russner, A. Weber, N.H. Menzler, O. Guillon, Boosting intermediate temperature performance of solid oxide fuel cells via a tri-layer ceria–zirconia–ceria electrolyte, J. Am. Ceram. Soc. 106 (1) (2022) 93–99, http://dx.doi.org/10.1111/jace.18482.

[9] M.P. Klitkou, A. Lopez de Moragas, J. Taubmann, S. Pirou, P. Khajavi, P.V. Hendriksen, H.L. Frandsen, Investigating viability of low temperature co-sintering to produce Ni-YSZ supported solid oxide electrolysis cells with a Ni-GDC active layer, Appl. Energy 400 (2025) 126547, http://dx.doi.org/10.1016/j.apenergy.2025.126547.

[10] A. Schwiers, C. Lenser, O. Guillon, N.H. Menzler, Interdiffusion at electrochemical interfaces between yttria-stabilized zirconia and doped ceria, J. Eur. Ceram. Soc. 43 (14) (2023) 6189–6199, http://dx.doi.org/10.1016/j.jeurceramsoc.2023.06.015.

[11] C. Lenser, J. Zhang, N. Russner, A. Weber, O. Guillon, N. Menzler, Electro-chemo-mechanical analysis of a solid oxide cell based on doped ceria, J. Power Sources 541 (2022) 231505, http://dx.doi.org/10.1016/j.jpowsour.2022.231505.

[12] L. Schöller, L. Wehner, D. Schneider, R. Schwaiger, B. Nestler, Virtual design of multilayered SOFC microstructures based on particle packing and spherical harmonics, Modelling Simul. Mater. Sci. Eng. 34 (4) (2026) 045013, http://dx.doi.org/10.1088/1361-651X/ae7138.

[13] C. Lenser, J. Zurek, D. Naumenko, C.-A. Thieu, J.-W. Son, U. de Haart, Q. Fang, L. Blum, N.H. Menzler, Performance analysis of a planar solid oxide fuel cell stack between 750 °C and 500 °C, J. Power Sources 474 (2020) 228671, http://dx.doi.org/10.1016/j.jpowsour.2020.228671.

[14] D. Klotz, A. Weber, E. Ivers-Tiffée, Practical guidelines for reliable electrochemical characterization of solid oxide fuel cells, Electrochim. Acta 227 (2017) 110–126, http://dx.doi.org/10.1016/j.electacta.2016.12.148.

[15] A. Weber, Testing of solid oxide cells at high current densities, Tm - Tech. Mess. 89 (2) (2022) 97–106, http://dx.doi.org/10.1515/teme-2021-0102.

[16] J.B.T.M. Roerdink, A. Meijster, The watershed transformation: Definitions, algorithms and parallelization strategies, Fund. Inform. 41 (2000) 187–228, http://dx.doi.org/10.3233/FI-2000-411207.

[17] G. Hamarneh, X. Li, Watershed segmentation using prior shape and appearance knowledge, Image Vis. Comput. (ISSN: 02628856) 27 (1–2) (2009) 59–68, http://dx.doi.org/10.1016/j.imavis.2006.10.009.

[18] M. Ender, J. Joos, A. Weber, E. Ivers-Tiffée, Anode microstructures from high-energy and high-power lithium-ion cylindrical cells obtained by X-ray nano-tomography, J. Power Sources (ISSN: 0378-7753) 269 (2014) 912–919, http://dx.doi.org/10.1016/j.jpowsour.2014.07.070.

[19] L.-Q. Chen, Phase-field models for microstructure evolution, Ann. Rev. Mater. Res. 32 (Volume 32, 2002) (2002) 113–140, http://dx.doi.org/10.1146/annurev.matsci.32.112001.132041.

[20] I. Steinbach, F. Pezzolla, B. Nestler, M. Seeßelberg, R. Prieler, G. Schmitz, J. Rezende, A phase field concept for multiphase systems, Phys. D: Nonlinear Phenom. 94 (3) (1996) 135–147, http://dx.doi.org/10.1016/0167-2789(95)00298-7.

[21] B. Nestler, H. Garcke, B. Stinner, Multicomponent alloy solidification: Phase-field modeling and simulations, Phys. Rev. E 71 (2005) 041609, http://dx.doi.org/10.1103/PhysRevE.71.041609.

[22] D. Schneider, F. Schwab, E. Schoof, A. Reiter, C. Herrmann, M. Selzer, T. Böhlke, B. Nestler, On the stress calculation within phase-field approaches: A model for finite deformations, Comput. Mech. 60 (2) (2017) 203–217, http://dx.doi.org/10.1007/s00466-017-1401-8.

[23] D. Schneider, E. Schoof, O. Tschukin, A. Reiter, C. Herrmann, F. Schwab, M. Selzer, B. Nestler, Small strain multiphase-field model accounting for configurational forces and mechanical jump conditions, Comput. Mech. 61 (3) (2018) 277–295, http://dx.doi.org/10.1007/s00466-017-1458-4.

[24] K. Rath, D. Herold, C. Melcher, A.K. Opitz, Chemical expansion data of GDC10 thin film and powder samples measured by in-situ XRD and HTXRD, 2025, http://dx.doi.org/10.5281/zenodo.17816329.

[25] I. Steinbach, Phase-field models in materials science, Modelling Simul. Mater. Sci. Eng. 17 (7) (2009) 073001, http://dx.doi.org/10.1088/0965-0393/17/7/073001.

[26] A. Prahs, L. Schöller, F.K. Schwab, D. Schneider, T. Böhlke, B. Nestler, A multiphase-field approach to small strain crystal plasticity accounting for balance equations on singular surfaces, Comput. Mech. 73 (4) (2024) 773–794, http://dx.doi.org/10.1007/s00466-023-02389-6.

[27] T. Kannenberg, L. Schöller, A. Prahs, D. Schneider, B. Nestler, Microstructure evolution accounting for crystal plasticity in the context of the multiphase-field method, Comput. Mech. 74 (1) (2024) 67–84, http://dx.doi.org/10.1007/s00466-023-02423-7.

[28] E. Schoof, D. Schneider, N. Streichhan, T. Mittnacht, M. Selzer, B. Nestler, Multiphase-field modeling of martensitic phase transformation in a dual-phase microstructure, Int. J. Solids Struct. (ISSN: 0020-7683) 134 (2018) 181–194, http://dx.doi.org/10.1016/j.ijsolstr.2017.10.032.

[29] Institute of Digital Materials Science (IDM), Karlsruhe University of Applied Sciences, Pace3D – a parallel phase-field framework, 2025, URL https://www.h-ka.de/en/idm/profile/pace3d-software. (Accessed 21 October 2025).

[30] S.G. Kim, D.I. Kim, W.T. Kim, Y.B. Park, Computer simulations of two-dimensional and three-dimensional ideal grain growth, Phys. Rev. E 74 (2006) 061605, http://dx.doi.org/10.1103/PhysRevE.74.061605.

[31] J. Hötzer, V. Rehn, W. Rheinheimer, M.J. Hoffmann, B. Nestler, Phase-field study of pore-grain boundary interaction, J. Ceram. Soc. Japan 124 (4) (2016) 329–339, http://dx.doi.org/10.2109/jcersj2.15266.

[32] B. Nestler, F. Wendler, M. Selzer, B. Stinner, H. Garcke, Phase-field model for multiphase systems with preserved volume fractions, Phys. Rev. E—Stat., Nonlinear, Soft Matter Phys. 78 (1) (2008) 011604.

[33] R.K. Jeela, A. Elmoghazy, L. Schöller, D. Schneider, B. Nestler, Effect of volume fractions and aging on Ni–GDC SOFC anode configurations on microstructural degradation and performance: multiphase-field simulations, npj Materials Degradation 10 (1) (2026) 82, http://dx.doi.org/10.1038/s41529-026-00811-x.

[34] I. Riess, Current-voltage relation and charge distribution in mixed ionic electronic solid conductors, J. Phys. Chem. Solids 47 (2) (1986) 129–138, http://dx.doi.org/10.1016/0022-3697(86)90121-6.

[35] M. Gödickemeier, L.J. Gauckler, Engineering of solid oxide fuel cells with ceria-based electrolytes, J. Electrochem. Soc. 145 (2) (1998) 414, http://dx.doi.org/10.1149/1.1838279.

[36] S. Dierickx, T. Mundloch, A. Weber, E. Ivers-Tiffée, Advanced impedance model for double-layered solid oxide fuel cell cermet anodes, J. Power Sources 415 (2019) 69–82, http://dx.doi.org/10.1016/j.jpowsour.2019.01.043.

[37] Q. Zhang, B.-K. Park, S. Barnett, P. Voorhees, On the role of the zirconia/ceria interface in the degradation of solid oxide electrolysis cells, Appl. Phys. Lett. 117 (12) (2020) 123906, http://dx.doi.org/10.1063/5.0016478.

[38] L. Wehner, Charakterisierung innovativer keramischer Materialien für Elektrolysezellen (Dissertation), RWTH Aachen University, Jülich, 2026, http://dx.doi.org/10.34734/FZJ-2026-02713.

[39] H.M. Ledbetter, R.P. Reed, Elastic properties of metals and alloys, I. Iron, nickel, and iron-nickel alloys, J. Phys. Chem. Ref. Data 2 (3) (1973) 531–618, http://dx.doi.org/10.1063/1.3253127.

[40] T. Kushi, K. Sato, A. Unemoto, S. Hashimoto, K. Amezawa, T. Kawada, Elastic modulus and internal friction of SOFC electrolytes at high temperatures under controlled atmospheres, J. Power Sources 196 (19) (2011) 7989–7993, http://dx.doi.org/10.1016/j.jpowsour.2011.05.040.

[41] G.W.C. Kaye, T.H. Laby, Tables of Physical and Chemical Constants and Some Mathematical Functions, twelveth ed., Longmans, Green, London, New York, 1959.

[42] J.N. Reddy, Mechanics of Laminated Composite Plates and Shells: Theory and Analysis, CRC Press, 2003.

[43] A. Nakajo, C. Stiller, G. Härkegård, O. Bolland, Modeling of thermal stresses and probability of survival of tubular SOFC, J. Power Sources 158 (1) (2006) 287–294, http://dx.doi.org/10.1016/j.jpowsour.2005.09.004.

[44] S. Watanabe, S. Sukino, T. Miyasaka, K. Sato, K. Yashiro, T. Kawada, T. Hashida, Influences of Ni content and porosity on mechanical properties of Ni–YSZ composites under solid oxide fuel cell operating conditions, J. Mater. Sci. 55 (20) (2020) 8679–8693, http://dx.doi.org/10.1007/s10853-020-04624-4.

[45] A. Müller-Bohn, eLamX^2: Open-source java composite calculator based on classical laminate theory, 2025, https://github.com/AndiMb/eLamX2. (Accessed 14 November 2025).

[46] L. Schöller, D. Schneider, C. Herrmann, A. Prahs, B. Nestler, Phase-field modeling of crack propagation in heterogeneous materials with multiple crack order parameters, Comput. Methods Appl. Mech. Engrg. 395 (2022) 114965, http://dx.doi.org/10.1016/j.cma.2022.114965.

[47] T. Akiba, S. Sano, T. Yanase, T. Ohta, M. Koyama, Optuna: A next-generation hyperparameter optimization framework, in: Proceedings of the 25th ACM SIGKDD International Conference on Knowledge Discovery and Data Mining, 2019.

[48] European Organization For Nuclear Research, OpenAIRE, Zenodo, 2013, http://dx.doi.org/10.25495/7GXK-RD71, URL https://www.zenodo.org/.

[49] L. Schöller, L. Wehner, D. Ramler, I. Kogut, S. Kucharski, C. Lenser, D. Schneider, A. Weber, R. Schwaiger, B. Nestler, Understanding electro-chemo-mechanical stresses in ceria-based solid oxide electrolysis cells using virtual microstructures – representative dataset, 2025, http://dx.doi.org/10.5281/zenodo.17789582.